

# Surface chemistry and nano/microstructure engineering on photocatalytic $\text{In}_2\text{S}_3$ nanocrystals

*Taisiia Berestok,<sup>†,‡</sup> Pablo Guardia,<sup>†</sup> Javier Blanco Portals,<sup>‡</sup> Sònia Estradé,<sup>‡</sup> Jordi Llorca,<sup>⊥</sup>  
Francesca Peiró,<sup>‡</sup> Andreu Cabot,<sup>†,⊥,\*</sup> Stephanie L. Brock,<sup>§,\*</sup>*

<sup>†</sup>Catalonia Institute for Energy Research – IREC, 08930 Sant Adrià de Besòs, Barcelona, Spain

<sup>‡</sup> LENS-MIND, Departament d'Enginyeries i Electrònica i Institut de Nanociència i  
Nanotecnologia (In2UB), Universitat de Barcelona, 08028, Barcelona, Spain

<sup>⊥</sup> Institut de Tècniques Energètiques, Universitat Politècnica de Catalunya, 08028 Barcelona,  
Spain

<sup>⊥</sup> ICREA, Pg. Lluís Companys 23, 08010 Barcelona, Spain

<sup>§</sup> Department of Chemistry, Wayne State University, Detroit, Michigan 48202, United States

KEYWORDS. Aerogel, xerogel,  $\text{In}_2\text{S}_3$ , dye degradation, photocatalytic activity, colloid,  
nanocrystal, nanomaterial.

ABSTRACT: Colloidal nanocrystals (NCs) compete with molecular catalysts in the field of  
homogenous catalysis, offering an easier recyclability and a number of potentially advantageous  
functionalities, such as tunable band gaps, plasmonic properties or a magnetic moment. Using  
high throughput printing technologies, colloidal NCs can be also supported onto substrates to

produce cost-effective electronic, optoelectronic, electrocatalytic and sensing devices. For both catalytic and technological application, NCs surface chemistry and supracrystal organization are key parameters determining final performance. Here, we study the influence of the surface ligands and the NC organization on the catalytic properties of  $\text{In}_2\text{S}_3$ , both in colloidal form and as a supported layer. In colloidal form, NCs stabilized in solution by inorganic ligands show the highest photocatalytic activities, which we associate with their large and more accessible surfaces. On the other hand, when NCs are supported on a substrate, their organization becomes an essential parameter determining performance. For instance, NC-based films produced through a gelation process provided five-fold higher photocurrent densities than those obtained from dense films produced by the direct printing of NCs.

## INTRODUCTION

Semiconductor nanocrystals (NCs) combine huge surface areas with a solid state platform for charge carrier photogeneration and transport.<sup>1</sup> This combination of properties makes them particularly appealing for applications involving interaction with the surrounding media, such as catalysis,<sup>2,3</sup> environmental remediation,<sup>4,5</sup> and sensing.<sup>6</sup> Colloidal NCs are especially suited for quasi-homogenous catalysis because relative to molecular catalysts they offer easier recyclability and added functionalities such as a magnetic moment for remote location or recovery, tunable band gaps for photocatalysis, and modulability to produce multisite systems by combining multiple co-catalysts.<sup>7,8</sup> However, the ability of colloidal NCs to interact with the surrounding media is controlled by their surface chemistry, which also determines several other fundamental properties, including colloidal and chemical stabilities and charge carrier and surface trap densities.<sup>9</sup> To find surface chemistries that simultaneously optimize all these parameters is extremely challenging and at the same time critical to exploit their full potential.

Colloidal NCs can be also assembled or supported within macroscopic structures and devices as required in electrocatalysis or sensing, for instance.<sup>10-12</sup> Beyond their huge surface area, solution processability, associated with high throughput and cost-effectiveness, is the main advantage of colloidal NCs in technological applications, especially when compared with thin films produced by vacuum-based technologies. When supported, a proper NC organization becomes essential to maintain their inherent large surface areas, while ensuring at the same time proper electrical conductivities for effective charge injection/extraction.<sup>13</sup> To face this key challenge, a plethora of approaches to engineer NC solids with controlled NC arrangement have been developed. A highly used approach involves slow NC assembly driven by an oversaturation of the NC concentration during solvent removal.<sup>14,15</sup> While yielding in some cases astonishing NC assemblies, this strategy does not generally provide materials with large surface areas and is strongly limited in terms of reproducibility, production throughput and scale up potential. To produce highly porous structures in a cost-effective manner, faster assembly strategies, based on destabilizing the NC dispersion in solution, are more suitable. This destabilization can be induced by externally triggering the ligand desorption or stimulating its binding.<sup>10,16</sup> The ultimate goal is to produce an interconnected NC network, i.e. a gel, with a proper surface chemistry to interact with the media.<sup>17</sup> In this direction, an effective approach to produce highly porous NC superstructures with good transport properties is the oxidative removal of thiolate ligands to link chalcogenide NCs through chalcogen-chalcogen bonds.<sup>18</sup> Following this approach, gels of different metal chalcogenides have been produced.<sup>19-21</sup>

$\text{In}_2\text{S}_3$  is an n-type semiconductor (2.6 eV band gap) with large exciton Bohr radius of 33.8 nm<sup>22</sup> used in lithium-ion batteries,<sup>23</sup> as photodetector,<sup>24</sup> for solar energy conversion through photocatalysis,<sup>25-27</sup> and particularly as a host material for two-photon absorption processes

through an intermediate band.<sup>28-29</sup> While its chemical stability, low defect density, simple synthesis, and proper band gap makes it an excellent candidate for photocatalytic applications, this material is yet underexplored in this area. There have been reported a number of synthetic procedures to produce  $\text{In}_2\text{S}_3$  NCs with different morphologies.<sup>[1-4]</sup> Ultrathin  $\text{In}_2\text{S}_3$  nanobelts showed promise for phosphorous displays due to the blue emission in photoluminescence spectra.<sup>[1]</sup> Doping of  $\text{In}_2\text{S}_3$  by Mn, Cu demonstrated tunable dual color emission at blue and orange depending on the excitation wavelength.<sup>[]</sup> Moreover it has been demonstrated that depending on the morphology of the NCs and facets enclosed,  $\text{In}_2\text{S}_3$  can serve as an efficient catalysts for dye degradation under either UV, visible or NIR light irradiation.<sup>[5]</sup> Furthermore, there have been reported several works devoted to improvement of photocatalytic performance via producing composites.  $\text{In}_2\text{O}_3/\text{In}_2\text{S}_3/\text{Ag}$  nanoheterostructures have been shown improved efficiency towards photoelectrochemical water splitting.<sup>[]</sup> However, to the best of our knowledge, the study on the influence of the  $\text{In}_2\text{S}_3$  NC surface chemistry has not been shown.

In this work, we evaluate the photocatalytic activity of colloidal  $\text{In}_2\text{S}_3$  NCs both in solution and when supported. We analyze the effect of different surface chemistries and NC organizations to determine the conditions resulting in best performances for quasi-homogeneous catalysis and photoelectrocatalysis.

## EXPERIMENTAL DETAILS

**Materials.** Indium trichloride ( $\text{InCl}_3$ , 98%), oleylamine (OAm, 70%), oleic acid (OAc, 90%), sulfur powder (99.998 %), 11-mercaptoundecanoic acid (MUA, 95%), tetramethylammonium hydroxide pentahydrate (TMAOH,  $\geq 97\%$ ), dodecanethiol (DDT,  $\geq 98\%$ ), tert-dodecanethiol (tDDT, 98.5 %), N-methylformamide (MFA, 99 %), phosphotungstic acid hydrate

( $\text{H}_3[\text{PW}_{12}\text{O}_{40}] \cdot x\text{H}_2\text{O}$ , PTA, 95 %), trifluoroacetic acid (TFA, 99 %), tetranitromethane (TNM, 95 %), rhodamine B (RhB, 97 %), sodium hydroxide (NaOH,  $\geq 98$  %), sodium sulfide ( $\text{Na}_2\text{S}$ ), and potassium chloride (KCl,  $\geq 99$  %) were purchased from Sigma-Aldrich. Hexane, methanol and acetone were of analytical grade and were purchased from Panreac. Glass substrates coated with indium tin oxide (ITO,  $\sim 8 \Omega/\text{sq}$ ) were acquired from VWR. Milli-Q water (MQ-Water): 18.2 M $\Omega$ , filtered with filter pore size 0.22  $\mu\text{M}$ , Millipore. All syntheses were carried out using standard air-free Schlenk-line techniques.

**Synthesis of  $\text{In}_2\text{S}_3$  NCs:** Among the several established synthetic protocols to produce  $\text{In}_2\text{S}_3$  NCs with different shapes and sizes,<sup>23-24,27,29</sup> we followed a slight variation of the procedure reported by K. H. Park et al.,<sup>30</sup> to obtain  $\text{In}_2\text{S}_3$  NCs with a two-dimensional disk-like morphology. The difference between the synthesis procedure reported by K. H. Park et al. and ours is that we used an injection step instead of a heating up procedure, since the latter led to a broader size-distribution in our hands (Figure S1 b). Briefly, in a 25 mL three-neck flask, 1 mmol of  $\text{InCl}_3$  and 10 mL of OAm were mixed and degassed ( $\sim 100$  mTorr) for 60 minutes at 80 °C under magnetic stirring. During this time, a clear solution formed. Then, the temperature was raised up to 220 °C (5 °C/min) and a previously degassed (15 minutes) solution containing 1.5 mmol of sulphur powder in 5 mL of OAm was swiftly injected. Upon injection of the sulphur precursor solution, the color of the solution gradually changed from transparent to orange, indicating the NC formation. After 10 minutes, the reaction was quenched by removing the heating mantle and placing the flask in a water bath. During the cooling step, the color of the solution changed from orange to yellow. NCs were precipitated by adding 30 mL of acetone to the crude solution and centrifuging the mixture at 5700 rpm for 5 min. The supernatant was discarded and the precipitate was redispersed in 5 mL of hexane. A second purification step was

performed following the same procedure. Finally, NCs were dispersed in 5 mL of hexane (~ 10 mg/mL solution) and stored for later use.

**Surface modification with PTA:** The procedure used to replace native organic ligands with PTA was based on previous work by J. Huang et al.<sup>31</sup> Briefly, 1 mL of a 10 mg/mL dispersion of In<sub>2</sub>S<sub>3</sub> NCs in hexane was mixed with 1 mL of a MFA solution that contained 20 mL of TFA and 50 mg (0.0173 mmols) of PTA. The formed biphasic solution was shook vigorously for 10 seconds and then stirred for 30-60 minutes. After stirring, the mixture was allowed to separate into the two phases. The migration of NCs from the upper hexane phase to the lower MFA phase indicated the ligand exchange and transfer of particles into a polar solvent. The upper liquid phase was discarded and then 2 mL of a hexane: acetone (1:1) mixture was added to the vial. The solution was then shook and centrifuged at 3000 rpm for 5 min. This step was repeated 3 times for the purpose of removing as much of the residual ligands as possible. Finally, the precipitated NCs were redispersed in MQ-Water for dye degradation measurements and in methanol for film preparation.

**Surface modification with InCl<sub>3</sub>:** The procedure used to replace native organic ligands with a In-Cl complex was based on previous work by V. Sayevich et al.<sup>32</sup> Basically, the same steps followed above to modify the In<sub>2</sub>S<sub>3</sub> NCs surface with PTA were used to modify them with InCl<sub>3</sub>, with two small differences: i) the 1 mL MFA solution contained 30 mg of InCl<sub>3</sub> (0.135 mmols); ii) to facilitate the phase transfer / ligand exchange, instead of TFA, 1 mL of acetone was additionally introduced in the initial biphasic solution before shaking. Finally, NCs were redispersed in MQ-Water or in methanol depending on whether they were to be used for dye degradation measurements or film preparation, respectively.

**Surface modification with MUA:** The procedure used to replace native organic ligands with MUA was based on a previous work by S. F. Wuister et al.<sup>33</sup> Briefly, 5 mL of a 20 mg/mL dispersion of In<sub>2</sub>S<sub>3</sub> NCs were mixed with 5 mL of a MUA solution (2 mM in methanol). The resulting biphasic solution was stirred under inert atmosphere for 30 min. During this time, NCs moved from the upper hexane phase to the bottom methanol phase. The upper part was removed and NCs were precipitated by addition of 30 mL of acetone and centrifuging at 4000 rpm for 5 min. The obtained precipitate was redispersed in methanol and precipitated one more time with acetone. NCs were finally dispersed in MQ-Water or methanol. It should be noted that repeating the washing procedure several more times led to NCs aggregation, but addition of few mL of the MUA solution (2 mM in methanol) permitted redispersion NCs back in solution.

**Direct NC deposition:** 1 mL of the hexane or methanol solution containing In<sub>2</sub>S<sub>3</sub> NCs (20 mg/mL) with the selected surface ligand (OAm, PTA, InCl<sub>3</sub>, MUA) was spin-coated on previously washed ITO substrates at a rotation speed of 2000 rpm for 20 seconds. The obtained films were annealed at 250 °C for 60 min under argon flow.

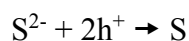
**NC deposition through xerogel formation:** 1 mL of MUA-capped In<sub>2</sub>S<sub>3</sub> NCs (20 mg/mL) in methanol was spin-coated on ITO substrates at a rotation speed of 2000 rpm for 20 seconds. Immediately after preparation, the film was dipped in a TNM solution (50 μL of 3% TNM in 5 mL of acetone) for 1 min. Subsequently, the film was rinsed with fresh methanol to remove by-products and then annealed at 250 °C for 60 min under argon flow.

**Gel and aerogel preparation:** The procedure used to produce In<sub>2</sub>S<sub>3</sub> NC gels and aerogels was based on our previous work.<sup>19</sup> To produce In<sub>2</sub>S<sub>3</sub> NC gels, 50 μL of a TNM solution (3% in acetone) were added into 2 mL of a methanol solution containing MUA-capped In<sub>2</sub>S<sub>3</sub> NCs (10 mg/mL). The mixture was shaken vigorously for 30 seconds and then kept undisturbed for the

whole gelation process. The gelation process visually evolved during 2 h, but the solution was left undisturbed for two days to ensure its completion. After two days, the solvent mixture (methanol and acetone) was exchanged to pure acetone, removing all the methanol and TNM residues. This process must be carried out with special care in order to not damage the porous network of the gel. At the same time, the solvent cannot be completely removed at any step. Thus, we partially replaced the solvent every 1-2 h for 2 days. While not optimized, relatively long time intervals between solvent replacements were used to ensure complete penetration of the fresh solvent into the porous structure of the gel. After the solvent exchange, the gel immersed in acetone was loaded into a supercritical point dryer chamber and soaked with liquid CO<sub>2</sub> overnight. After 12 h, the chamber was half drained and filled with fresh liquid CO<sub>2</sub>. This procedure was repeated at least 6 times in one-hour intervals in order to replace acetone by liquid CO<sub>2</sub>. Finally, the chamber was completely filled with liquid CO<sub>2</sub> and heated to 39 °C. Upon heating, the pressure increased up to 75-80 bars, thus surpassing the supercritical point of CO<sub>2</sub>. The sample was kept under these conditions for 1 h. Afterward, the pressure was released while keeping the temperature constant.

**Dye degradation experiments:** The photocatalytic activity of In<sub>2</sub>S<sub>3</sub> NCs was evaluated by photodegradation of RhB. In a typical experiment, 1 mL of an aqueous RhB solution (100 ppm) was added to 9 mL of an aqueous solution containing In<sub>2</sub>S<sub>3</sub> NCs (1.1 mg/mL). Before reaction, the mixture was kept in the dark for 30 min under magnetic stirring. Then, the glass reaction vessel was exposed through its open top to a 300 W xenon lamp for 2 h providing ca. 100 mW/cm<sup>2</sup> irradiance at the sample.

**Photoelectrochemical measurements:** The photoelectrocatalytic activity of In<sub>2</sub>S<sub>3</sub> NCs was evaluated through the photoelectrochemical oxidation of a polysulfide electrolyte:<sup>34</sup>



the oxidized species,  $\text{S}_x^{2-}$ , is converted back (reduced) to  $\text{S}^{2-}$  on the counter electrode:



Photocurrent measurements were performed using a three-electrode cell configuration with a Pt-coiled wire having a surface area of  $2 \text{ cm}^2$  as a counter electrode and an Ag/AgCl reference electrode filled with 3M KCl solution. A 1M aqueous solution of S, NaOH and  $\text{Na}_2\text{S}$  at pH7 was used as electrolyte. A bias voltage to the working electrode was applied through an electrical contact to the uncoated part of the ITO-glass substrate. A surface area of  $1 \text{ cm}^2$  of the deposited film was in contact with the electrolyte. Illumination was provided by 8 xenon lamps (35 W each) radially distributed with a total power of 280 W and irradiance on the sample of ca.  $100 \text{ mW/cm}^2$ . Electrochemical impedance spectroscopy (EIS) was performed using versaSTAT3. Measurements were conducted in the frequency range from 100 kHz to 1 mHz with a 5 mV Ac amplitude using the three-electrode cell configuration with the same conditions used for photocurrent measurements.

**Characterization techniques:** Transmission electron microscopy (TEM) characterization was carried out using a ZEISS LIBRA 120, operating at 120 kV. Samples were prepared by drop casting a diluted NC solution onto a carbon coated copper grid (200 mesh). Scanning electron microscopy (SEM) analysis was carried out using a ZEISS Auriga microscope. For SEM characterization, NCs were dispersed in appropriate solvent and drop casted onto silicon substrates. X-ray power diffraction (XRD) analyses were carried out on a Bruker AXS D8 ADVANCE X-ray diffractometer with Ni-filtered ( $2 \mu\text{m}$  thickness) Cu  $\text{K}\alpha_1$  radiation ( $\lambda = 1.5406 \text{ \AA}$ ). For XRD analysis, NCs in solution were drop casted (200-500  $\mu\text{L}$  at a concentration

of about 3 mg/mL) onto a zero-signal silicon wafer. UV-vis absorption spectra were recorded on a PerkinElmer LAMBDA 950 UV-vis spectrophotometer. Samples were prepared by diluting 100  $\mu$ L in 2 mL of hexane inside a 10 mm path length quartz cuvette. UV-vis diffuse reflectance spectra were acquired with a Jasco V-570 UV/Vis/NIR spectrophotometer equipped with an integrating sphere. The solid sample was placed on the sample holder and measured from 1000 to 300 nm and the baseline was corrected using a BaSO<sub>4</sub> reflectance standard. The Kubelka-Munk equation was employed to convert reflectance to absorption.<sup>34</sup> FTIR spectra were recorded from 500  $\text{cm}^{-1}$  to 4000  $\text{cm}^{-1}$  using a PerkinElmer FT-IR 2000 spectrophotometer. Dynamic light scattering (DLS) measurements were performed using a Zeta Sizer (Malvern Instruments) equipped with a 4.0 mW HeNe laser operating at 633 nm and an avalanche photodiode detector. For DLS analysis, samples were diluted in 2 mL of appropriate solvent inside a 10 mm path length glass cuvette. X-ray photoelectron spectroscopy (XPS) measurements were carried out on a SPECS system equipped with an Al anode XR50 source operating at 150 mW and a Phoibos 150 MCD-9 detector. The pressure in the analysis chamber was kept below  $10^{-7}$  Pa. The area analyzed was about 2 mm x 2 mm. The pass energy of the hemispherical analyzer was set at 25 eV and the energy step was maintained at 1.0 eV. Data processing was performed with the Casa XPS program (Casa Software Ltd., UK). Binding energies were shifted according to the reference C 1s peak that was located at 284.8 eV. The fitting of each component was performed taking into account the characteristic width of each peak (taking into account the particular element and electronic state) and the separation of each doublet as reported in the Handbook of X-ray photoelectron spectroscopy [REF]. Thermogravimetric analyses (TGA) were carried out using PerkinElmer Diamond TG/DTA instrument. For TG analysis, samples were dried and 20

mg of the dried powder was loaded into a ceramic pan. Measurements were carried out in an Ar atmosphere from ambient temperature to 500 °C at a heating rate of 2 °C/min.

## RESULTS AND DISCUSSIONS

Figure 1a displays a representative TEM micrograph of the  $18 \pm 2$  nm  $\text{In}_2\text{S}_3$  NCs produced through the injection of a OAm-sulfur solution into a hot (220 °C) OAm solution containing  $\text{InCl}_3$ , as described in the experimental section. Using this synthetic protocol, a slight variation of that reported by K. H. Park et al.,<sup>30</sup>  $\beta\text{-In}_2\text{S}_3$  NCs with disk-like morphology were produced. The thickness of the  $\text{In}_2\text{S}_3$  nanodisks was previously reported at 0.76 nm,<sup>30</sup> which corresponds to a single unit cell, and their diameter could be adjusted in the range from 18 nm to 90 nm by using different sulfur precursors and/or reaction times (see details in the supporting information, SI, Figure S1).

The XRD patterns of the as-synthesized NCs and NC aerogel displayed the reflections of the  $\beta\text{-In}_2\text{S}_3$  with tetragonal crystal structure (Figure 2 a). Two intense peaks observed on the diffraction patterns suggest the preferential growth along these planes. However, we did not observe (0012) and (1015) peaks which indicates about retardant growth rate along these lattice planes. Similar trend was reported by Park et al for  $\text{In}_2\text{S}_3$  nanoplates.[] The assembly of NCs into aerogel did not affect the material crystallinity. However, the diffraction pattern from the aerogel sample is appeared to be noisier. This might be due to the aerogel porous nature.

Figure 2 b shows the absorption spectra of the as-synthesized OAm-NCs and NC aerogel converted from the spectra obtained using diffuse reflectance UV-vis spectroscopy. Measurements demonstrated slight shift of the absorption peak for the aerogel sample suggesting

the changes in the NCs sizes upon gelation. Indeed calculation of the NCs sizes using Scherrer equation demonstrated the decrease in the size values from  $L_{(311)} = 18$  nm for precursor NCs to  $L_{(311)} = 15$  nm for NC aerogel. This indicates that the changes in the band gap originated from the quantum confinement effects. These results are consistent with the one obtained for CdSe NC aerogels and can indicate about the etching of the NCs surface during the process of gelation.[<sup>6</sup>] Furthermore the difference in the absorption between NCs and aerogel can be due to aerogel interconnected structure and different powders packing and delocalization along the network.[<sup>7</sup>] Similar trend was observed by Brock et al, for CdSe NCs where the various aerogel density resulted in the absorption shift.[<sup>8</sup>]

The presence of OAm in the reaction mixture was fundamental to produce  $\text{In}_2\text{S}_3$  crystals with sizes in the nanometer size regime and with narrow size and shape distributions. OAm binds indium ions at the NCs surface, limiting the access/reaction of additional monomer and thus confining the NC growth. At the same time, OAm molecules bound at the NC surface colloiddally stabilized them during synthesis, enabling their homogeneous growth. The presence of OAm was indicated by FTIR analysis (Figure 2 c), and was expected to modulate the NC catalytic activity.

To determine the effect of surface ligands on the photocatalytic properties of  $\text{In}_2\text{S}_3$  NCs and to direct their assembly, OAm was replaced from as-produced NCs (OAm-NCs) with three different ligands: a composition-matched inorganic ligand, In-Cl complex (InCl-NCs); a non-matching inorganic ligand,  $(\text{PW}_{12}\text{O}_{40})^{3-}$  ( $(\text{PW}_{12}\text{O}_{40})^3$ -NCs); and a shorter organic ligand, MUA (MUA-NCs). In all cases, new ligands were introduced using previously reported two-phase methods adapted to our system.<sup>31,32</sup>

In brief, to replace the native OAm with inorganic ligands, a hexane solution containing the  $\text{In}_2\text{S}_3$  NCs was mixed with a PTA/TFA solution in MFA or with an  $\text{InCl}_3$  solution in MFA. This

process rendered the NCs soluble in polar media such as methanol or H<sub>2</sub>O, as confirmed by TEM and DLS measurements (Figure 1 c, d) which confirms successful ligand displacement of long-chain hydrocarbon organic ligands by smaller one or inorganic. FTIR spectra from the functionalized NCs demonstrated the absence of the peaks at 2800-2900 cm<sup>-1</sup> assigned to the C-H vibration band from OAm (Figure 2 c), suggesting successful replacement of the native ligands.

The surface of In<sub>2</sub>S<sub>3</sub> NCs capped with InCl, (PW<sub>12</sub>O<sub>40</sub>)<sup>3-</sup>, and MUA ligands was characterized by the presence of negatively charged species, which resulted in negative ζ-potential values of -19 mV, -26 mV and -28 mV, respectively (Figure 1 e). TGA analysis further confirmed OAm displacement. (PW<sub>12</sub>O<sub>40</sub>)<sup>3-</sup>-NCs showed 9% weight loss, much lower close to 50% loss for OAm-NCs, (Figure 1 f).

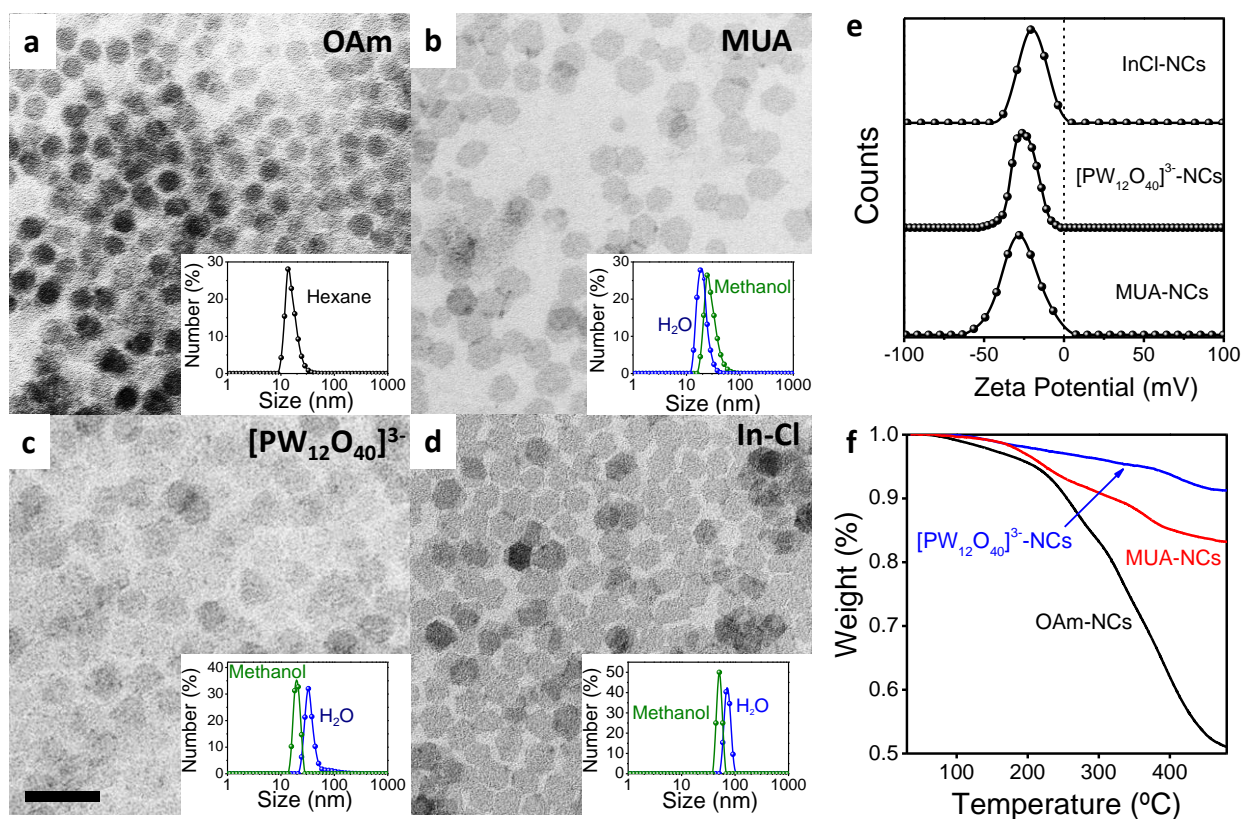


**Figure 1.** a-d) Representative TEM micrographs and corresponding DLS spectra of the initial  $\text{In}_2\text{S}_3$  NCs (a) and of the  $\text{In}_2\text{S}_3$  NCs capped with MUA (b),  $(\text{PW}_{12}\text{O}_{40})^{3-}$  (c), and an In-Cl complex (d). All micrographs have the same scale bar = 50 nm. e) Z-potential measurements of the  $\text{In}_2\text{S}_3$  NCs capped with MUA,  $(\text{PW}_{12}\text{O}_{40})^{3-}$ , and the In-Cl complex. e) TGA profiles of the initial  $\text{In}_2\text{S}_3$  NCs (OAm-NCs) and of the  $\text{In}_2\text{S}_3$  NCs capped with MUA and  $(\text{PW}_{12}\text{O}_{40})^{3-}$ .

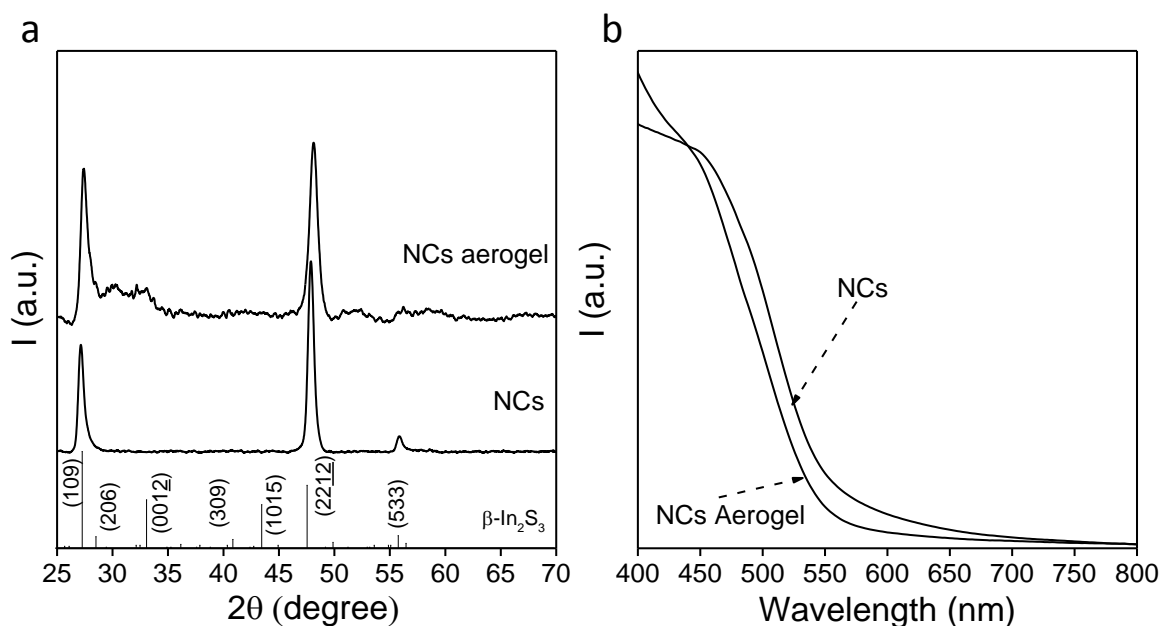


**Figure 2.** XRD patterns of the  $\text{In}_2\text{S}_3$  NCs and aerogel (a). The bars in the bottom correspond to the bulk  $\beta$ -  $\text{In}_2\text{S}_3$  (JCPDS N 25-0390). Absorption spectra for the NC powder and NC aerogel (b).

XPS measurements corroborated the presence of  $(\text{PW}_{12}\text{O}_{40})^{3-}$  and Cl on the surface of  $\text{In}_2\text{S}_3$  NCs (Figure 2). The XPS spectrum of  $(\text{PW}_{12}\text{O}_{40})^{3-}$ -NCs displayed the presence of tungsten at the  $\text{In}_2\text{S}_3$  NC surface ( $\sim 1\%$ ), with a main oxidation state compatible with that of a tungstate (W 4f<sub>7/2</sub> binding energy = 35.8 eV, Figure 2a).<sup>35</sup> The ratio In/S in  $(\text{PW}_{12}\text{O}_{40})^{3-}$ -NCs was slightly above that of stoichiometric  $\text{In}_2\text{S}_3$ : In/S = 0.87, and the main contribution to the In 3d<sub>5/2</sub> electronic states (77 %) displayed a relatively high binding energy (In 3d<sub>5/2</sub> binding energy

=446.1 eV) compared to that of  $\text{In}_2\text{S}_3$ , which would be compatible with a higher electronegativity of  $(\text{PW}_{12}\text{O}_{40})^{3-}$  anions.

The XPS spectrum of  $\text{In}_2\text{S}_3$  NCs stabilized with  $\text{InCl}_3$  (InCl-NCs) displayed the presence of Cl (~ 3%) in a metal chloride environment (Cl  $2p_{3/2}$  binding energy = 198.9 eV, Figure 2b). Additionally, the surface of InCl-NCs contained an even larger excess of In: In/S = 1.0. The main contribution to In electronic states (70 %) was compatible with both an  $\text{In}_2\text{S}_3$  and an InCl chemical environment (In  $3d_{5/2}$  binding energy = 445.2 eV, Figure 2b), and a minor component at (In  $3d_{5/2}$  binding energy = 445.8 eV) might be assigned to  $\text{InCl}_3$ .<sup>36</sup>

OAm was replaced with MUA by mixing  $\text{In}_2\text{S}_3$  NCs in hexane with a MUA solution in methanol.<sup>16</sup> This process rendered the  $\text{In}_2\text{S}_3$  NCs soluble in polar media such as methanol, isopropanol or water (Figure 1 b). FTIR spectra of  $\text{In}_2\text{S}_3$  NCs stabilized with MUA (MUA-NCs) showed the presence of peaks at  $2924\text{ cm}^{-1}$  and  $2830\text{ cm}^{-1}$  that correspond to C-H stretching (Figure 3 c). However, due to the shorter chain length of MUA compared with OAm, the intensity of these peaks was lower than in the initial OAm-stabilized  $\text{In}_2\text{S}_3$  NCs (OAm-NCs). This was consistent with TGA measurements that confirmed the decrease in organics amount (Figure 1 f). The as-synthesized NCs contained a large quantity of organics which was confirmed by weight loss of 50 %. The decrease in the loss up to 18% for MUA-NCs indicated less amount of organic of the NCs surface since MUA has lower molecular weight. And in the case of inorganic ligand functionalized  $(\text{PW}_{12}\text{O}_{40})^{3-}$ -NCs, the weight loss was 8%. Furthermore, in the FTIR spectra we observed the decrease in the intensity of the C-H peaks that come from organics. The disappearance of the weak peak at  $2547\text{ cm}^{-1}$  present in the spectrum of pure MUA, and which was attributed to the S-H stretching, indicated the binding of the ligand to the metal atom through the thiolate group. Finally, the peaks at  $1547\text{ cm}^{-1}$  and  $1406\text{ cm}^{-1}$  observed in

the FTIR spectrum of the MUA-NCs were attributed to the asymmetric and symmetric vibrational bands of the carboxylate, again consistent with the presence of the MUA functional group.

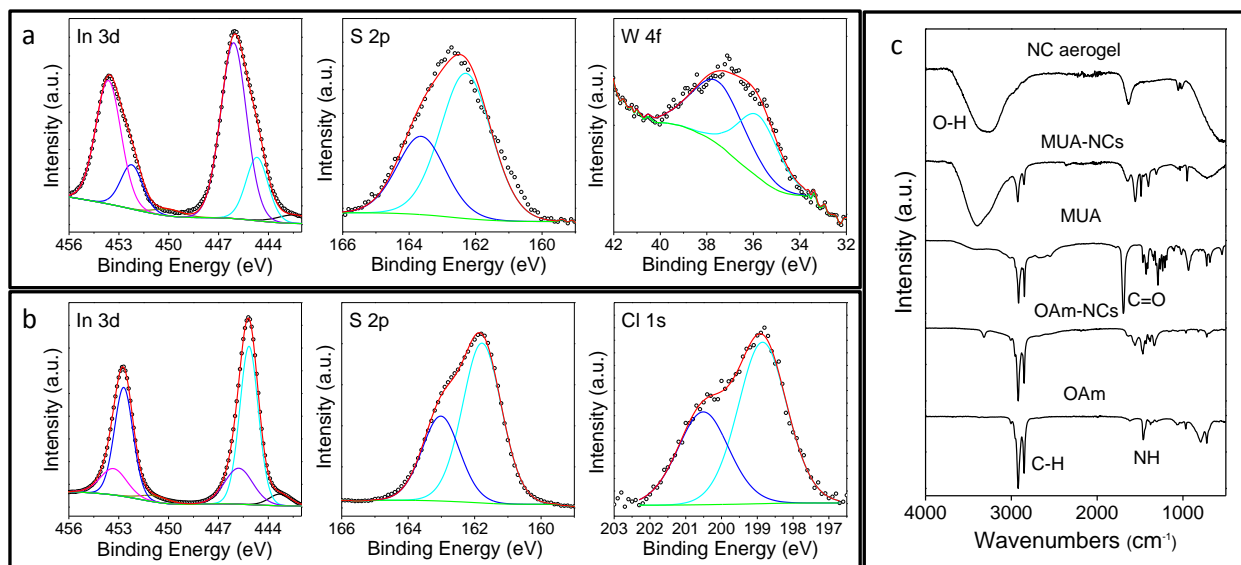


**Figure 3.** a) XPS spectrum of the In 3d, S 2p and Cl 1s regions obtained from  $(PW_{12}O_{40})^{3-}$ -NCs. b) XPS spectrum of the In 3d, S 2p and Cl 1s regions obtained from InCl-NCs. c) FTIR spectra of OAm, MUA, MUA-NCs, OAm-NCs and a NC aerogel. Note that MUA-NCs and OAm-NCs were dispersed in methanol and hexane respectively.

MUA-NCs were used as building blocks to produce  $In_2S_3$  gels (Figure 4). The assembly of MUA-NCs was triggered by exposing them to a non-oxygen-transferring oxidant, TNM (3% TNM solution in methanol).<sup>37</sup> As previously described,<sup>18</sup> TNM oxidized the thiolate ligands bound to  $In^{3+}$  ions at the NC surface producing disulfides. Upon thiolate displacement from the NC surface,  $In^{3+}$  ions at the NC surface can be easily solvated by the carboxylate species or methanol, leaving a chalcogen-rich NC surface. In such chalcogen-rich NCs, and in the presence of sufficient oxidizer, chalcogen catenation takes place, resulting in the aggregation of the NCs

into a network held together by interparticle chalcogen–chalcogen bonding.<sup>17</sup> This ligand-free gelation mechanism allows for direct connection of NCs without any intermediary ligand that could hinder, for instance, inter-particle charge transfer.

The formed gel was subsequently dried under super-critical CO<sub>2</sub> to retain the porous structure. TEM characterization of the resulting aerogel (Figures 4 a and S2) revealed the random aggregation of the NCs. However, HRTEM micrographs showed some of the attached NCs to have coincident crystallographic orientations (Figure S2). SEM characterization of aerogels suggested a highly porous three dimensional structure with large voids (Figure 4 b). FTIR analysis of the final aerogel evidenced that the gelation process was accompanied by the removal of MUA as proven by the suppression of the 2800-2900 cm<sup>-1</sup> peak corresponding to the C-H vibration band (Figure 3 c). The peak with low intensity at 2400 cm<sup>-1</sup> can be ascribed to vibration of C=O ketone group originated from carboxylate group of MUA.

The amount of oxidizing agent introduced was a key parameter controlling the gelation process. On one hand, low amounts of TNM resulted in partial NC aggregation and precipitation but without the formation of a proper NC network. On the other hand, an excess of the oxidizing agent resulted in much denser gels by strongly accelerated the NC aggregation through efficiently removing all the MUA molecules and leading to extensive chalcogen-chalcogen bond formation (Figure S3).

Type IV nitrogen adsorption/desorption isotherms, characteristic of mesoporous structures, were observed for the NC aerogels (Figure 4 d). From the fitting of the data to a Brunauer-Emmett-Teller (BET) model,<sup>38</sup> the surface area of In<sub>2</sub>S<sub>3</sub> NC aerogels was determined to be ca. 134 m<sup>2</sup>/g, while that of precipitated MUA-NCs was just 40 m<sup>2</sup>/g (Figure 4 d). For comparison,

the calculated surface area for colloidal  $\text{In}_2\text{S}_3$  NCs with a disk-like geometry, a thickness of 1 nm and a diameter of 18 nm was  $225 \text{ m}^2/\text{g}$ .

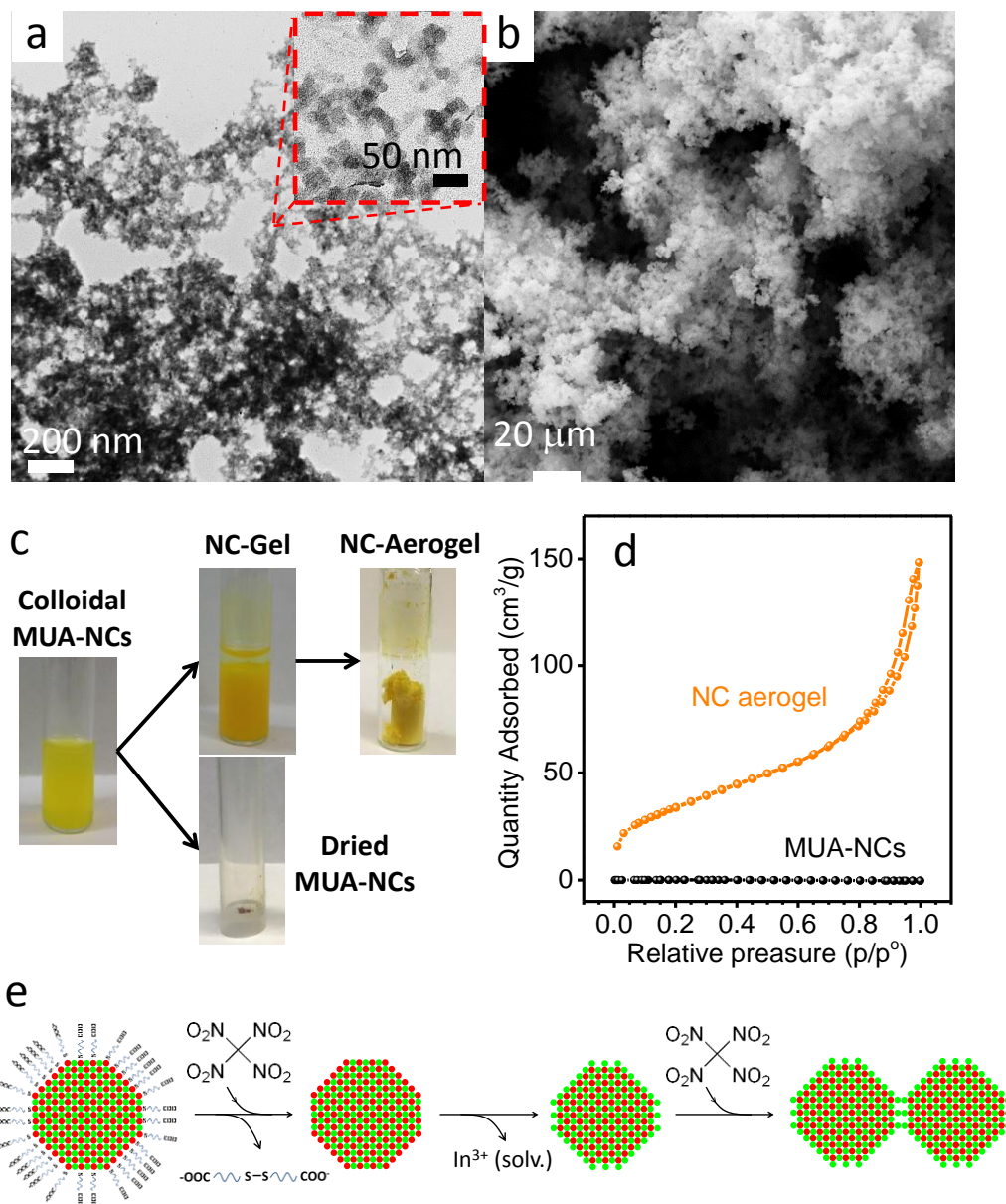


**Figure 4.** a) TEM and b) SEM micrographs of an  $\text{In}_2\text{S}_3$  NC aerogel. c) Vials containing the MUA-NC solution in methanol, a NC wet gel, the super-critically dried NCs aerogel and the precipitated and dried MUA-NCs. d) Nitrogen adsorption/desorption isotherms of an  $\text{In}_2\text{S}_3$  NC

aerogel and of dried MUA-NCs. e) Scheme of the gel formation by TNM oxidation of MUA and sulphur ions at the NC surface.

Due to absorption in the UV and visible region,  $\text{In}_2\text{S}_3$  is considered as a suitable candidate for photodegradation of dyes. There have been published several studies on the photocatalytic degradation of methylene blue,<sup>[9]</sup> methylene orange<sup>[10]</sup> and rhodamine B<sup>[11]</sup> over  $\text{In}_2\text{S}_3$  NCs (Table S1). In this work as an example it was decided to choose RhB.

The photocatalytic performance of  $\text{In}_2\text{S}_3$  NCs in suspension was evaluated through the degradation of RhB under xenon lamp irradiation (300 W). In a typical measurement, 20 mg of NCs were suspended in 10 mL of MQ-water containing 10 ppm of RhB. Before irradiation, the solution was stirred in the dark for 30 min to achieve adsorption equilibrium. Note that OAm-NCs were not stable in MQ-water and thus were not tested for RhB degradation. MUA-NCs showed a poor activity toward photodegradation of RhB, reaching just 50% of RhB degradation after 2 h illumination (Figure 5). We associated this poor performance to the limited access of RhB to the MUA-covered NC surface. Under illumination, photogenerated electrons are transferred to adsorbed dye molecules to decompose them. If not properly extracted, photogenerated holes accumulate at the  $\text{In}_2\text{S}_3$  NC and result in the oxidation of the NC surface.<sup>11</sup> In MUA-NCs, this photooxidation results in the detachment of MUA ligands as disulphides and, hence, induce irreversible NCs aggregation and consequent surface loss.<sup>39-41</sup>

$(\text{PW}_{12}\text{O}_{40})^{3-}$  and InCl-NCs provided the highest RhB degradation rates, which we attributed to the superior surface accessibility on these NCs due to the absence of organic ligands and their fair stability in solution during the whole experiment (Figure 5). No photooxidation-induced aggregation was observed for  $(\text{PW}_{12}\text{O}_{40})^{3-}$ -NCs and InCl-NCs proving the presence of these ligands to provide a better stability. Noteworthy, the  $\text{In}_2\text{S}_3$  NC-gel showed intermediate

efficiency for RhB degradation (65 %) under the same experimental conditions. This intermediate efficiency of NC-gels corresponded to a partially organic-free surface compared to MUA-NCs but associated with a lower total active area if compared with colloidal  $(PW_{12}O_{40})^{3-}$ -NCs and InCl-NCs. Compare to the work published by Liu et al.,<sup>11</sup> the  $(PW_{12}O_{40})^{3-}$ -NCs exhibit higher efficiency, even considering the fact that the amount of the catalyst used was significantly lower. The complete degradation of RhB was achieved in 210 min over  $In_2S_3$  nanotubes, however, in our case already in 120 min we observed the diminishing of RhB over inorganically functionalized NCs.

Furthermore, we compared the produced  $In_2S_3$  NC catalysts with  $In_2S_3$  bulk. As it was expected bulk  $In_2S_3$  exhibit moderate results compared to nanocrystalline material. We investigated the performance of  $In_2S_3$  NC aerogel compared to the catalytic performance with a  $TiO_2$  nanopowder as well.  $TiO_2$  is a common material used for photocatalytic energy conversion. However,  $TiO_2$  nanopowder showed lower catalytic activity under visible light irradiation compared to inorganically functionalized  $In_2S_3$  NCs.

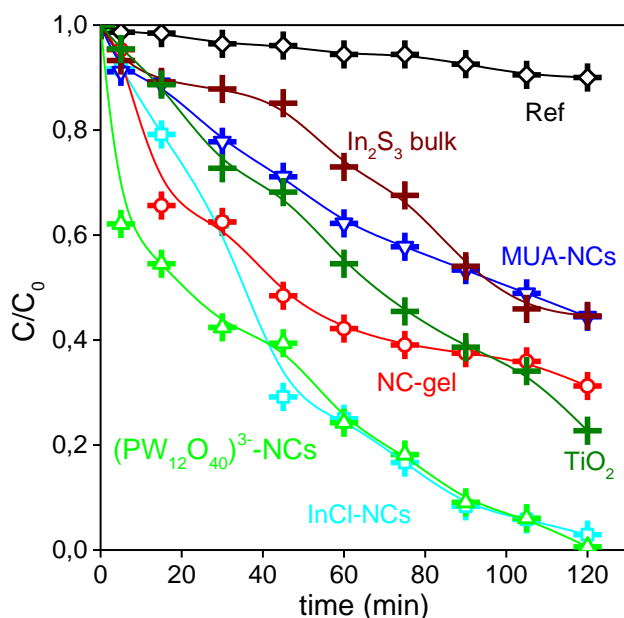


**Figure 5.** Photocatalytic degradation curves of RhB on MUA-NCs,  $(PW_{12}O_{40})^{3-}$ -NCs, InCl-NCs and a NC-gel. Experiments were carried out by irradiating a 10 ppm RhB mixture containing 20 mg of sample in MQ-water with a xenon lamp (300 W) for 2 hours.

To investigate their photoelectrocatalytic properties,  $In_2S_3$  NCs were supported on ITO-covered glass substrates. NC layers were prepared by spin coating a methanol solution of the NCs (Figure 6). To produce porous films, the MUA-NC layer was dipped into a TNM solution immediately after spin coating, interconnecting in this way the  $In_2S_3$  NCs into a porous network.<sup>20</sup> The substrate was afterwards rinsed with methanol to remove excess of TNM and reaction by-products. All layers were annealed at 250 °C for 60 min under argon flow before photoelectrocatalytic characterization.

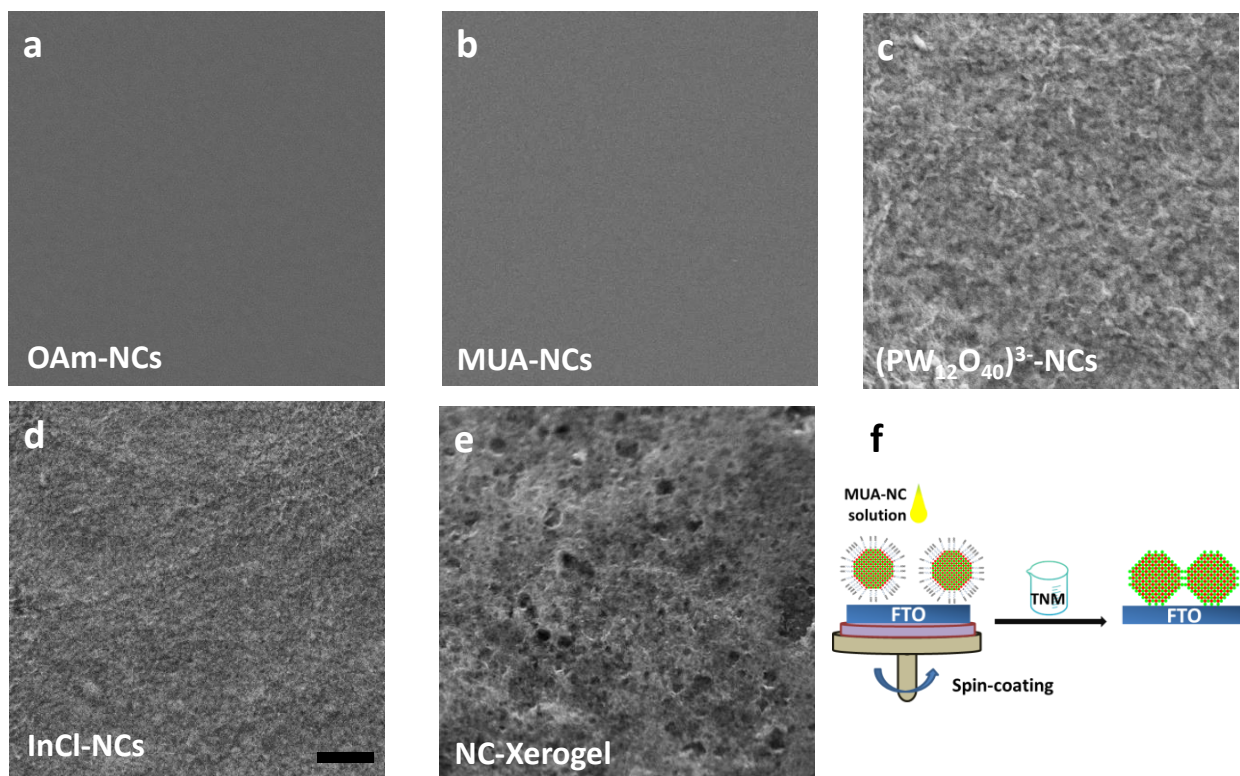


**Figure 6.** a-e) SEM images of films obtained by spin-coating OAm-NCs (a), MUA-NCs (b),  $(PW_{12}O_{40})^{3-}$ -NCs (c), InCl-NCs (d), and MUA-NCs that were subsequently linked together by oxidation with TNM to produce a xerogel film (e). Scale bar = 2  $\mu$ m. f) Scheme of the process of formation of a xerogel film.

The photoelectrocatalytic performance of  $In_2S_3$  NCs was evaluated using a three-electrode cell with a Pt-coiled counter electrode, an Ag/AgCl reference electrode and the NCs film as working electrode. A polysulfide solution, consisting of a 1 M aqueous solution of  $Na_2S$ , NaOH and S, was used as electrolyte. Figure 7 shows the results obtained from linear sweep voltammograms and time-dependent photocurrent measurements of the different samples analysed.

Films obtained by spin coating OAm- and MUA-NCs showed the lowest performance. We attribute this poor performance to a limited access of the sulphide species to the NC's surface and to the low electrical conductivity of the film due to the presence of the insulating organic ligands. The lower performance of OAm-NCs if compared to MUA-NCs could result from the hydrophobic nature of OAm-NCs which may reduce the interaction with the reaction solution hence reducing the current density. The hydrophilic nature of MUA-NC films provided a better contact between the NCs and the electrolyte and hence slightly higher photocurrent densities. Layers produced from  $(PW_{12}O_{40})^{3-}$ -NCs and InCl-NCs showed improved photocurrents compared with OAm-NCs, which we attributed to a more efficient charge transfer with the media and a faster charge transport between the NCs. Surprisingly, xerogel films provided the highest photocurrent densities, reaching 150  $\mu A/cm^2$  at 1.0 V vs Ag/AgCl which represent a five-fold increase compared to the  $(PW_{12}O_{40})^{3-}$ -NCs and InCl-NCs films (Figure 7 a). We attributed such enhanced performance of the xerogel films to: i) an organic-free NC interconnection, resulting in improved interaction and charge transfer, ii) a high degree of

porosity offering large active surface areas for interaction with the media. EIS measurements confirmed the lower charge transfer resistance of the xerogel layers compared with  $(PW_{12}O_{40})^{3-}$ -NCs and InCl-NCs films, associated again to the higher surface area of the interconnected NC of the xerogel films (Figure 7 c).

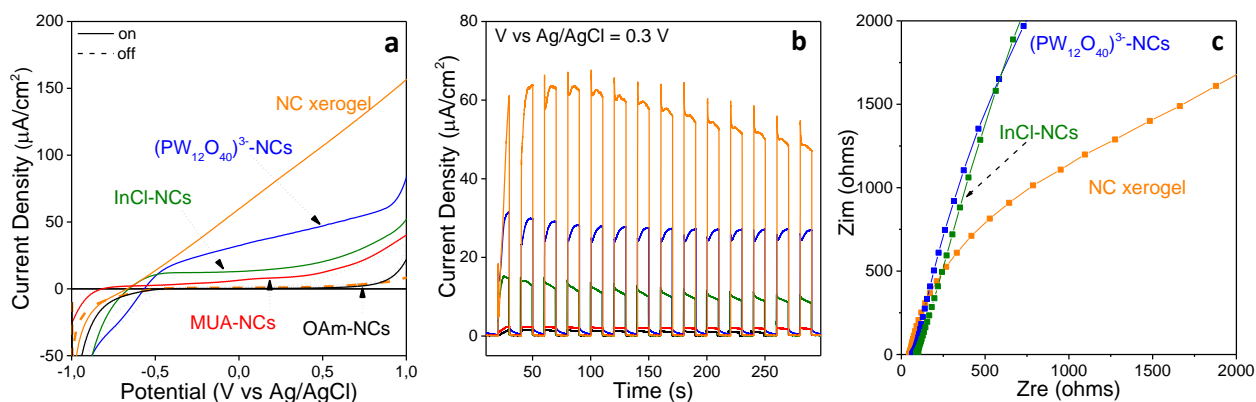


**Figure 7.** Linear sweep voltammogram curves (a) and chronoamperometric characteristics normalized by the amount of photoactive material at 0.3 V vs. Ag/AgCl (b) of xerogel layers and layers produced from OAm-, MUA-,  $(PW_{12}O_{40})^{3-}$ - and InCl-NCs. Nyquist plots for  $(PW_{12}O_{40})^{3-}$ - and InCl-NCs and xerogel layer (c).

## CONCLUSIONS

We compared the photocatalytic and photoelectrocatalytic performance of 18 nm disk-shaped  $In_2S_3$  NCs with different surface chemistries and supra-crystalline organization. Dispersions of  $In_2S_3$  NCs, colloidally stabilized with inorganic ligands such as polyoxometallates or chlorides, showed the highest photocatalytic performance toward dye degradation in solution. We attributed this experimental fact to the higher accessibility of the NC surface provided by the

inorganic ligands compared with the organic ones and to the colloidal stability of the materials, which provided maximized surface areas to interact with the media. On the other hand, organized NC assemblies provided higher photoelectrocatalytic performances than organic- and inorganic-capped NCs. The organization of the NCs into networks held together through chalcogen-chalcogen bonds simultaneously provided larger surface areas for interaction with the media compared with layers of precipitated NCs, and effective avenues for charge transport through the layer.

## ASSOCIATED CONTENT

### **Supporting Information**

The Supporting Information is available free of charge at DOI:

Additional experimental details. TEM images of  $\text{In}_2\text{S}_3$  NCs with different sizes and shapes.

Optical photographs of  $\text{In}_2\text{S}_3$  NC-gel obtained using different amount of TNM. HRTEM

analysis. Band gap determination. Chronoamperometric characteristics obtained from NC-

xerogel films with different thickness

## AUTHOR INFORMATION

### **Corresponding Authors**

\*E-mail: [acabot@irec.cat](mailto:acabot@irec.cat)

\*E-mail: [sbrock@chem.wayne.edu](mailto:sbrock@chem.wayne.edu)

## ACKNOWLEDGMENT

This work was supported by the European Regional Development Funds and the Spanish MINECO project BOOSTER. TB thanks FI-AGAUR Research Fellowship Program, Generalitat de Catalunya (2015 FI\_B 00744). PG acknowledges the People Programme (Marie Curie Actions) of the FP7/2007-2013 European Union Program (TECNIOspring grant agreement no. 600388) and the Agency for Business Competitiveness of the Government of Catalonia, ACCIÓ. SB acknowledges the U.S. National Science Foundation, CHE-1361741.

## ABBREVIATIONS

NC, nanocrystal; OAm, oleylamine; OAc, oleic acid; MUA, 11-mercaptopundecanoic acid; TMOH, tetramethylammonium hydroxide pentahydrate; DDT, dodecanethiol; tDDT, tert-dodecanethiol; MFA, n-methylformamide; PTA, phosphotungstic acid hydrate; TFA, trifluoroacetic acid; TNM, tetranitromethane; RhB, rhodamine B; ITO, indium tin oxide; TEM, transmission electron microscopy; HRTEM, high-resolution TEM; SEM, scanning electron microscopy; UV-vis, ultraviolet-visible spectroscopy; UV/vis/NIR, ultraviolet-visible near infrared spectroscopy; X-ray power diffraction (XRD); DLS, dynamic light scattering; FTIR, Fourier-transform infrared spectroscopy; XPS, X-ray photoelectron spectroscopy; ICP, inductively coupled plasma mass spectroscopy; OAm-NCs, OAm-capped NCs;  $(\text{PW}_{12}\text{O}_{40})^{3-}$ -NCs,  $(\text{PW}_{12}\text{O}_{40})^{3-}$ -capped NCs; InCl-NCs, InCl-capped NCs; MUA-NCs, MUA-capped NCs.

## REFERENCES

- (1) Talapin, D. V.; Lee, J.-S.; Kovalenko, M. V.; Shevchenko, E. V., Prospects of colloidal nanocrystals for electronic and optoelectronic applications. *Chem. Rev.* **2010**, *110*, 389-458.
- (2) Popczun, E. J.; McKone, J. R.; Read, C. G.; Biacchi, A. J.; Wiltrout, A. M.; Lewis, N. S.; Schaak, R. E., Nanostructured nickel phosphide as an electrocatalyst for the hydrogen evolution reaction. *J. Am. Chem. Soc.* **2013**, *135*, 9267-9270.

- (3) Li, D.; Baydoun, H.; Kulikowski, B.; Brock, S. L., Boosting the catalytic performance of iron phosphide nanorods for the oxygen evolution reaction by incorporation of manganese. *Chem. Mat.* **2017**, *29*, 3048-3054.
- (4) Thatai, S.; Khurana, P.; Boken, J.; Prasad, S.; Kumar, D., Nanoparticles and core-shell nanocomposite based new generation water remediation materials and analytical techniques: A review. *Microchem. J.* **2014**, *116*, 62-76.
- (5) Yu, X.; Shavel, A.; An, X.; Luo, Z.; Ibáñez, M.; Cabot, A., Cu<sub>2</sub>ZnSnS<sub>4</sub>-Pt and Cu<sub>2</sub>ZnSnS<sub>4</sub>-Au heterostructured nanoparticles for photocatalytic water splitting and pollutant degradation. *J. Am. Chem. Soc.* **2014**, *136*, 9236-9239.
- (6) Mahmoud, M. A.; O'Neil, D.; El-Sayed, M. A., Hollow and solid metallic nanoparticles in sensing and in nanocatalysis. *Chem. Mat.* **2014**, *26* (1), 44-58.
- (7) Zhang, Q.; Su, H.; Luo, J.; Wei, Y., A magnetic nanoparticle supported dual acidic ionic liquid: a "quasi-homogeneous" catalyst for the one-pot synthesis of benzoxanthenes. *Green Chem.* **2012**, *14*, 201-208.
- (8) Xiang, Q.; Yu, J.; Jaroniec, M., Synergetic effect of MoS<sub>2</sub> and graphene as cocatalysts for enhanced photocatalytic h<sub>2</sub> production activity of TiO<sub>2</sub> nanoparticles. *J. Am. Chem. Soc.* **2012**, *134*, 6575-6578.
- (9) Talapin, D. V., Nanocrystal solids: A modular approach to materials design. *MRS Bull.* **2012**, *37*, 63-71.
- (10) Stolarczyk, J. K.; Deak, A.; Brougham, D. F., Nanoparticle clusters: assembly and control over internal order, current capabilities, and future potential. *Adv. Mater.* **2016**, *28*, 5400-5424.

- (11) Korala, L.; Germain, J. R.; Chen, E.; Pala, I. R.; Li, D.; Brock, S. L., CdS aerogels as efficient photocatalysts for degradation of organic dyes under visible light irradiation. *Inorg. Chem. Front.* **2017**, *4*, 1451-1457.
- (12) Wu, Z.-S.; Yang, S.; Sun, Y.; Parvez, K.; Feng, X.; Müllen, K., 3D nitrogen-doped graphene aerogel-supported Fe<sub>3</sub>O<sub>4</sub> nanoparticles as efficient electrocatalysts for the oxygen reduction reaction. *J. Am. Chem. Soc.* **2012**, *134*, 9082-9085.
- (13) Kagan, C. R.; Lifshitz, E.; Sargent, E. H.; Talapin, D. V., Building devices from colloidal quantum dots. *Science* **2016**, *353*, 6302.
- (14) Shevchenko, E. V.; Talapin, D. V.; Kotov, N. A.; O'Brien, S.; Murray, C. B., Structural diversity in binary nanoparticle superlattices. *Nature* **2006**, *439*, 55.
- (15) Redl, F. X.; Cho, K. S.; Murray, C. B.; O'Brien, S., Three-dimensional binary superlattices of magnetic nanocrystals and semiconductor quantum dots. *Nature* **2003**, *423*, 968.
- (16) Gaponic, N.; Herrmann, A.-K.; Eychmüller, A., Colloidal Nanocrystal-Based Gels and Aerogels: Material Aspects and Application Perspectives. *J. Phys. Chem. Lett.* **2012**, *3*, 8-17.
- (17) Mohanan, J. L.; Arachchige, I. U.; Brock, S. L., Porous Semiconductor Chalcogenide Aerogels. *Science* **2005**, *307*, 397-400.
- (18) Pala, I. R.; Arachchige, I. U.; Georgiev, D. G.; Brock, S. L., reversible gelation of ii–vi nanocrystals: the nature of interparticle bonding and the origin of nanocrystal photochemical instability. *Angew. Chem. Int. Edit.* **2010**, *49*, 3661-3665.
- (19) Arachchige, I. U.; Brock, S. L., Sol–gel methods for the assembly of metal chalcogenide quantum dots. *Accounts Chem. Res.* **2007**, *40*, 801-809.

- (20) Korala, L.; Wang, Z.; Liu, Y.; Maldonado, S.; Brock, S. L., Uniform thin films of CdSe and CdSe(ZnS) Core(Shell) quantum dots by sol-gel assembly: enabling photoelectrochemical characterization and electronic applications. *ACS Nano* **2013**, *7*, 1215-1223.
- (21) Korala, L.; Li, L.; Brock, S. L., Transparent conducting films of CdSe(ZnS) core(shell) quantum dot xerogels. *Chem. Commun.* **2012**, *48*, 8523-8525.
- (22) Gschneidner, K.A.; Eyring, Jr. and L. *Handbook on the Physics and Chemistry of Rare Earths*; Gschneidner, K.A.; Eyring, Jr. and L., Eds.; Elsevier, 1999; Vol. 11, p.148.
- (23) Peng, S.; Li, L.; Wu, Y.; Jia, L.; Tian, L.; Srinivasan, M.; Ramakrishna, S.; Yan, Q.; Mhaisalkar, S. G., Size- and shape-controlled synthesis of ZnIn<sub>2</sub>S<sub>4</sub> nanocrystals with high photocatalytic performance. *CrystEngComm* **2013**, *15*, 1922-1930.
- (24) Xie, X.; Shen, G., Single-crystalline In<sub>2</sub>S<sub>3</sub> nanowire-based flexible visible-light photodetectors with an ultra-high photoresponse. *Nanoscale* **2015**, *7*, 5046-5052.
- (25) He, Y.; Li, D.; Xiao, G.; Chen, W.; Chen, Y.; Sun, M.; Huang, H.; Fu, X., A New application of nanocrystal In<sub>2</sub>S<sub>3</sub> in efficient degradation of organic pollutants under visible light irradiation. *J. Phys. Chem. C* **2009**, *113*, 5254-5262.
- (26) Xu, R.; Li, H.; Zhang, W.; Yang, Z.; Liu, G.; Xu, Z.; Shao, H.; Qiao, G., The fabrication of In<sub>2</sub>O<sub>3</sub>/In<sub>2</sub>S<sub>3</sub>/Ag nanocubes for efficient photoelectrochemical water splitting. *Phys. Chem. Chem. Phys.* **2016**, *18*, 2710-2717.
- (27) Du, W.; Zhu, J.; Li, S.; Qian, X., Ultrathin β-In<sub>2</sub>S<sub>3</sub> Nanobelts: Shape-Controlled Synthesis and Optical and Photocatalytic Properties. *Cryst. Growth Des.* **2008**, *8*, 2130-2136.
- (28) Lucena, R.; Aguilera, I.; Palacios, P.; Wahnón, P.; Conesa, J. C., Synthesis and spectral properties of nanocrystalline V-substituted In<sub>2</sub>S<sub>3</sub>, a novel material for more efficient use of solar radiation. *Chem. Mat.* **2008**, *20*, 5125-5127.

- (29) Tapia, C.; Berglund, S. P.; Friedrich, D.; Dittrich, T.; Bogdanoff, P.; Liu, Y.; Levchenko, S.; Unold, T.; Conesa, J. C.; De Lacey, A. L.; Pita, M.; Fiechter, S., Synthesis and characterization of V-doped  $\beta$ -In<sub>2</sub>S<sub>3</sub> thin films on FTO substrates. *J. Phys. Chem. C* **2016**, *120*, 28753-28761.
- (30) Park, K. H.; Jang, K.; Son, S. U., Synthesis, Optical properties, and self-assembly of ultrathin hexagonal In<sub>2</sub>S<sub>3</sub> nanoplates. *Angew. Chem. Int. Edit.* **2006**, *45*, 4608-4612.
- (31) Huang, J.; Liu, W.; Dolzhnikov, D. S.; Protesescu, L.; Kovalenko, M. V.; Koo, B.; Chattopadhyay, S.; Shenchenko, E. V.; Talapin, D. V., Surface functionalization of semiconductor and oxide nanocrystals with small inorganic oxoanions (PO<sub>4</sub><sup>3-</sup>, MoO<sub>4</sub><sup>2-</sup>) and polyoxometalate ligands. *ACS Nano* **2014**, *8*, 9388-9402.
- (32) Sayevich, V.; Guhrenz, C.; Sin, M.; Dzhagan, V. M.; Weiz, A.; Kasemann, D.; Brunner, E.; Ruck, M.; Zahn, D. R. T.; Leo, K.; Gaponik, N.; Eychmüller, A., Chloride and indium-chloride-complex inorganic ligands for efficient stabilization of nanocrystals in solution and doping of nanocrystal solids. *Adv. Funct. Mat.* **2016**, *26*, 2163-2175.
- (33) Wuister, S. F.; de Mello Donegá, C.; Meijerink, A., Influence of thiol capping on the exciton luminescence and decay kinetics of CdTe and CdSe quantum dots. *J. Phys. Chem. B* **2004**, *108*, 17393-17397.
- (34) Yang, Z.; Chen, C.-Y.; Roy, P.; Chang, H.-T., Quantum dot-sensitized solar cells incorporating nanomaterials. *Chem. Commun.* **2011**, *47*, 9561-9571.
- (35) Tauc, J.; Grigorovici, R.; Vancu, A., Optical properties and electronic structure of amorphous germanium. *Phys. Status Solidi B* **1966**, *15*, 627-637.
- (36) Moulder, J. F.; Stickle, W. F.; Sobol, P. E.; Bomben, K. D. Handbook of X-Ray Photoelectron Spectroscopy; Perkin-Elmer: Eden Prairie, MN, 1992.

- (37) Evans, B. J.; Takahashi Doi, J.; Kenneth Musker W.,  $^{19}\text{F}$  NMR study of the reaction of p-fluorobenzenethiol and disulfide with periodate and other selected oxidizing agents. *J. Org. Chem.* **1990**, *55*, 2337.
- (38) Sing K. S. W., Reporting physisorption data for gas/solid systems with special reference to the determination of surface area and porosity, *Pure Appl. Chem.* **1982**, *54*, 2201.
- (39) Simon, T.; Bouchonville, N.; Berr, M. J.; Vaneski, A.; Adrović, A.; Volbers, D.; Wyrwich, R.; Döblinger, M.; Susha, A. S.; Rogach, A. L.; Jäckel, F.; Stolarczyk, J. K.; Feldmann, J., Redox shuttle mechanism enhances photocatalytic  $\text{H}_2$  generation on Ni-decorated CdS nanorods. *Nat. Mater.* **2014**, *13*, 1013.
- (40) Aldana, J.; Wang, Y. A.; Peng, X., Photochemical Instability of CdSe Nanocrystals Coated by Hydrophilic Thiols. *J. Am. Chem. Soc.* **2001**, *123*, 8844-8850.
- (41) Rogach, A. L.; Kornowski, A.; Gao, M.; Eychmüller, A.; Weller, H., Synthesis and characterization of a size series of extremely small thiol-stabilized CdSe nanocrystals. *J. Phys. Chem. B* **1999**, *103*, 3065-3069.